PAPER • OPEN ACCESS

Transport of a colloidal particle driven across a temporally oscillating optical potential energy landscape

To cite this article: Joshua L Abbott *et al* 2019 *New J. Phys.* **21** 083027

View the article online for updates and enhancements.

New Journal of Physics

The open access journal at the forefront of physics

CrossMark

OPEN ACCESS

PAPER

Transport of a colloidal particle driven across a temporally oscillating optical potential energy landscape

Joshua L Abbott[1], **Arthur V Straube**[2,3], **Dirk G A L Aarts**[1] **and Roel P A Dullens**[1] ⓘ

[1] Department of Chemistry, Physical and Theoretical Chemistry Laboratory, University of Oxford, South Parks Road, Oxford, OX1 3QZ, United Kingdom
[2] Freie Universität Berlin, Department of Mathematics and Computer Science, Arnimalle 6, D-14195 Berlin, Germany
[3] Group 'Dynamics of Complex Materials', Zuse Institute Berlin, Takustr. 7, D-14195 Berlin, Germany

E-mail: roel.dullens@chem.ox.ac.uk

Keywords: dynamic mode locking, colloids, optical potential energy landscape, optical trapping, nonlinear dynamics
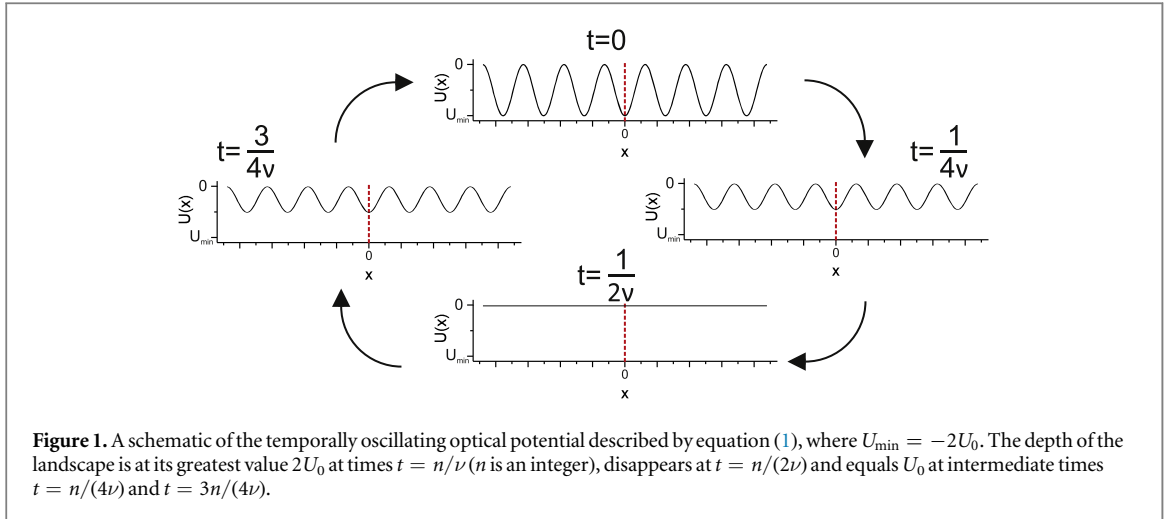
Abstract

A colloidal particle is driven across a temporally oscillating one-dimensional optical potential energy landscape and its particle motion is analysed. Different modes of dynamic mode locking are observed and are confirmed with the use of phase portraits. The effect of the oscillation frequency on the mode locked step width is addressed and the results are discussed in light of a high-frequency theory and compared to simulations. Furthermore, the influence of the coupling between the particle and the optical landscape on mode locking is probed by increasing the maximum depth of the optical landscape. Stronger coupling is seen to increase the width of mode locked steps. Finally, transport across the temporally oscillating landscape is studied by measuring the effective diffusion coefficient of a mobile particle, which is seen to be highly sensitive to the driving velocity and mode locking.

1. Introduction

Rough surfaces are inherent to everyday life, and on the macroscopic scale can range from tectonic plates [1] to the soles of running shoes [2]. Despite many surfaces seeming smooth, at the microscopic scale every surface has some level of roughness [3, 4], which leads to phenomena that are often not obvious as an extension from the macroscopic world. Surface roughness, for instance, gives rise to complex ad-atomic motion across a crystal surface [5, 6], the creation of kinks and antikinks [7, 8], and can act as a source of templated crystal growth [9, 10]. Further examples of rough surfaces appear in the form of sinusoidal potential energy landscapes in superconductors and have direct applications in Josephson junctions [11], vortex motion [12] and charge density waves [13]. These systems are inherently hard to image [14], making studying them challenging.

Creating a model system of colloidal particles in an optical potential energy landscape leads to a far more accessible system with increased control. Particle motion across random potential energy landscapes has led to observed subdiffusion [15–20], which can be controlled with surface roughness [15]. Exact particle motion has been shown to heavily rely on the form of the landscape and can give rise to freely diffusive as well as trapped particles [16, 21]. Further to this, the study of colloidal particle transport across periodic potential energy surfaces has led to many interesting observations such as subdiffusion [22, 23], superdiffusion [23–26], ballistic motion [26, 27] and synchronisation [28–30]. Structured surfaces have also been created to achieve precise particle sorting [31, 32] or directed transport [33, 34].

On the colloidal scale, studies of time-dependent potential energy landscapes have exhibited rich dynamics such as accelerated motion with low dispersion [35, 36] and a reduction in static friction [37] due to mode locking. Conversely, time-dependence can also cause enhanced diffusion [26, 27, 38] and, under the correct conditions, can lead to bidirectional particle transport [39]. Experiments carried out for large systems subject to a time-dependent optical potential energy landscape show that collective effects, such as kinks, can affect the dynamics [37]. Precise control of mean drift and enhanced diffusion of colloidal particles can be achieved in traveling potential energy landscapes [40, 41]. Single particle behaviour in temporally oscillating potentials has

Figure 1. A schematic of the temporally oscillating optical potential described by equation (1), where $U_{\min} = -2U_0$. The depth of the landscape is at its greatest value $2U_0$ at times $t = n/\nu$ (n is an integer), disappears at $t = n/(2\nu)$ and equals U_0 at intermediate times $t = n/(4\nu)$ and $t = 3n/(4\nu)$.

also been probed theoretically in terms of velocity and diffusion [35], though systematic single particle experiments are lacking.

Here we drive a colloidal particle through a temporally oscillating optical potential energy landscape and analyse trajectories to quantify the nature of transport. As in a system with a natural internal frequency under external temporal modulation, the competition between the corresponding internal and external frequencies may cause a synchronised or dynamically mode locked regime of motion [42]. Synchronisation is indeed observed and can be directly visualised in the form of phase portraits. We study the effect of the oscillation frequency as well as the effect of altering the coupling between the particle and the oscillating landscape on the synchronisation behaviour. This is achieved through changing the maximum depth of the optical potential energy landscape. We also characterise the efficiency of particle transport by analysing the effective diffusion coefficient whilst altering the driving velocity and the coupling between the particle and the oscillating landscape.

2. Theoretical background

2.1. Langevin equation

To model the temporally oscillating optical potential energy landscape we consider a line of equally spaced traps. At small trap separations the spatial dependence of the landscape is known to be sinusoidal [43]. The laser power is assumed to change sinusoidally with time with a period ν^{-1}, where ν is the external frequency. The overall evolution of the landscape is sketched in figure 1. The roughness of the potential is at its greatest at the time period and vanishes at half the time period. Note that since laser power is non-negative, the positions of the minima and maxima are stationary in space and do not interchange. Thus, the spatio-temporal dependence of the temporally oscillating optical potential energy landscape can be cast into a simple expression

$$U_{\mathrm{opt}}(x, t) = -2U_0 \cos^2(\pi\nu t) \cos^2\left(\frac{\pi x}{\lambda}\right), \tag{1}$$

where U_0 is the amplitude of the landscape and λ its wavelength.

A particle driven through this temporally oscillating one-dimensional optical potential energy landscape (1) experiences the force $F(x, t) = F_{\mathrm{DC}} + F_{\mathrm{opt}}(x, t)$, where F_{DC} is the constant driving force and $F_{\mathrm{opt}} = -\partial U_{\mathrm{opt}}/\partial x$. As a result, the overdamped motion of this colloidal sphere is described by the Langevin equation

$$\zeta \frac{\mathrm{d}x}{\mathrm{d}t} = F_{\mathrm{DC}} - \frac{F_{\mathrm{C}}}{2}(1 + \cos\omega t)\sin kx + \xi(t), \tag{2}$$

where $x(t)$ is the particle position, ζ is the friction coefficient, λ is the wavelength, $k = 2\pi/\lambda$ is the wavenumber and $\omega = 2\pi\nu$ is angular frequency with ν the frequency. The critical force of the static optical landscape is given by $F_{\mathrm{C}} = kU_0$, and $\xi(t)$ is the irregular force accounting for thermal fluctuations. The latter is modelled as Gaussian white noise with zero mean $\langle \xi(t) \rangle = 0$ and variance $\langle \xi(t)\xi(t') \rangle = 2\zeta k_B T\delta(t - t')$, where $k_B T$ is the thermal energy.

2.2. Average velocity and effective diffusion

To characterise transport of our system we use the average velocity and the effective diffusion coefficient. The average velocity can be obtained as asymptotic drift velocity

$$v_{\mathrm{AV}} = \lim_{t \to \infty} \frac{\langle X(t) \rangle}{t}, \tag{3}$$

where $X(t) = x(t) - x(0)$ and the angular brackets denote the ensemble average. As in [29], we expect that the average velocity at the dynamic mode locking steps is given by the resonance condition $v_{\mathrm{AV}} = n\lambda\nu$, where n is an integer step number. This condition follows from the requirement of frequency locking $\nu_{\mathrm{AV}} = n\nu$, meaning that the observed (average) frequency ν_{AV} is a multiple of the external frequency ν. The effective diffusion coefficient D_{eff} is evaluated as [25]

$$D_{\mathrm{eff}} = \lim_{t \to \infty} \frac{\delta x^2(t)}{2t} \tag{4}$$

with the mean squared displacement $\delta x^2(t) = \langle X^2(t) \rangle - \langle X(t) \rangle^2$.

3. Experimental methods

3.1. Colloidal model system

The colloidal model system used consists of Dynabeads M-270 Carboxylic Acid that have a diameter of 3 μm when dispersed in 20% EtOH(aq). These are held in a quartz glass Hellma cell (internal cavity, 20 mm $\times$ 9 mm $\times$ 200 μm) and the particles have a higher mass density than the surrounding solvent so sediment to the bottom of the cell [29]. The gravitational length of our particles is about 0.06 μm , which is only 2% of their diameter. Therefore, after sedimentation this is effectively a quasi two-dimensional system. The system is sufficiently dilute to ensure that there is only a single particle in the field of view at any time. The diffusion coefficient for a free particle $D_0 = k_B T / \zeta \approx 0.04 \ \mu\mathrm{m}^2 \ \mathrm{s}^{-1}$ [28].

3.2. Experimental setup

The sample is imaged and manipulated using an optical setup described in [44] that consists of a brightfield microscope coupled to a 1064 nm infrared laser. The laser light is focused at the sample plane and controlled using a pair of AODs. The particles are tracked in real time at 40 fps. A line of optical traps is used to form a sinusoidal optical landscape [29] with a wavelength of $\lambda = 3.5 \ \mu$m . The laser power is varied between $I_0 = 200$–480 mW corresponding to the critical velocity $v_{\mathrm{C}} = F_{\mathrm{C}} / \zeta = 2.1$–4.7 μm s^{-1}, where $I_0 \propto v_{\mathrm{C}}$ (as $F_{\mathrm{C}} \propto U_0 \propto I_0$).

3.3. Oscillating the depth of the optical landscape

The landscape depth is oscillated sinusoidally as described in section 2.1 with a frequency of $\nu = 0.1$–1.0 Hz . For each combination of laser power and frequency, a scan of driving velocities is carried out to obtain particle trajectories from which the average velocity is calculated. Importantly, this calculation is carried out for a time period corresponding to an integer number of oscillations of the optical landscape depth.
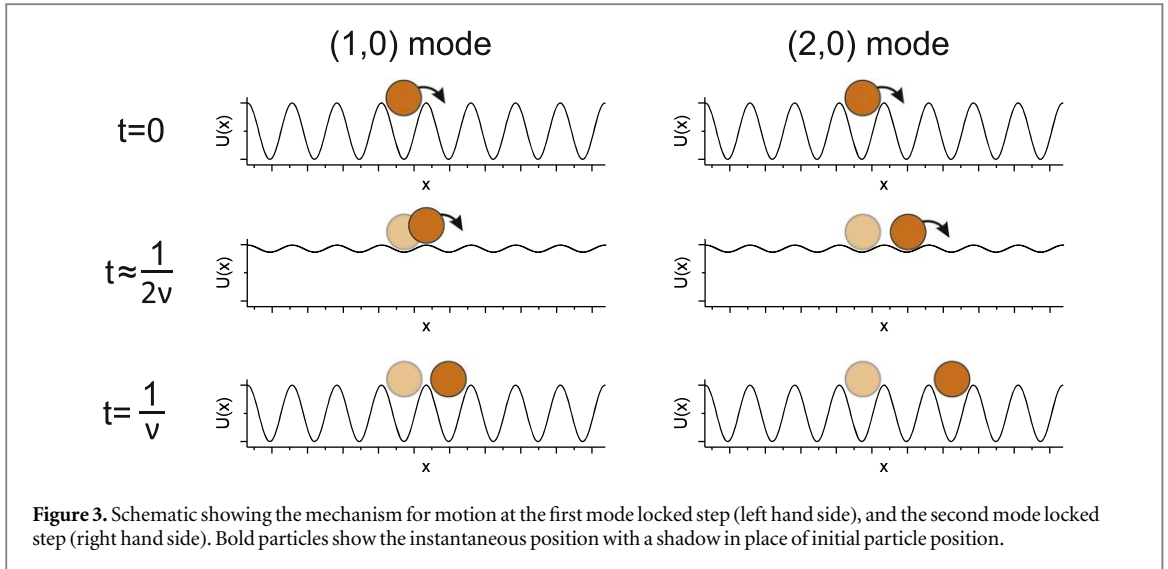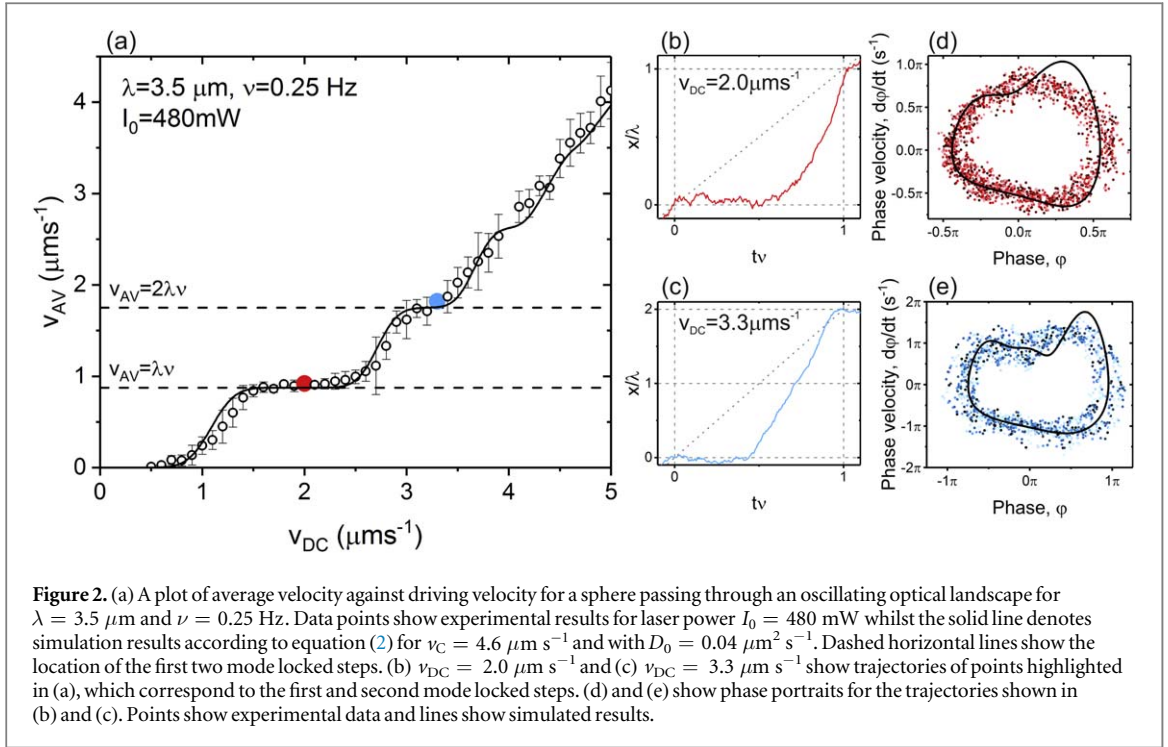
3.4. Step widths

The width of the mode locked steps is analysed from the experimentally measured average velocity. A mode locked step is here defined as having an average velocity equal to $v_{\mathrm{AV}} = n\lambda\nu \pm 0.1 \times (n\lambda\nu)$ and containing at least two data points. This threshold is chosen to ensure that the full width of a step is captured.

4. Results and discussion
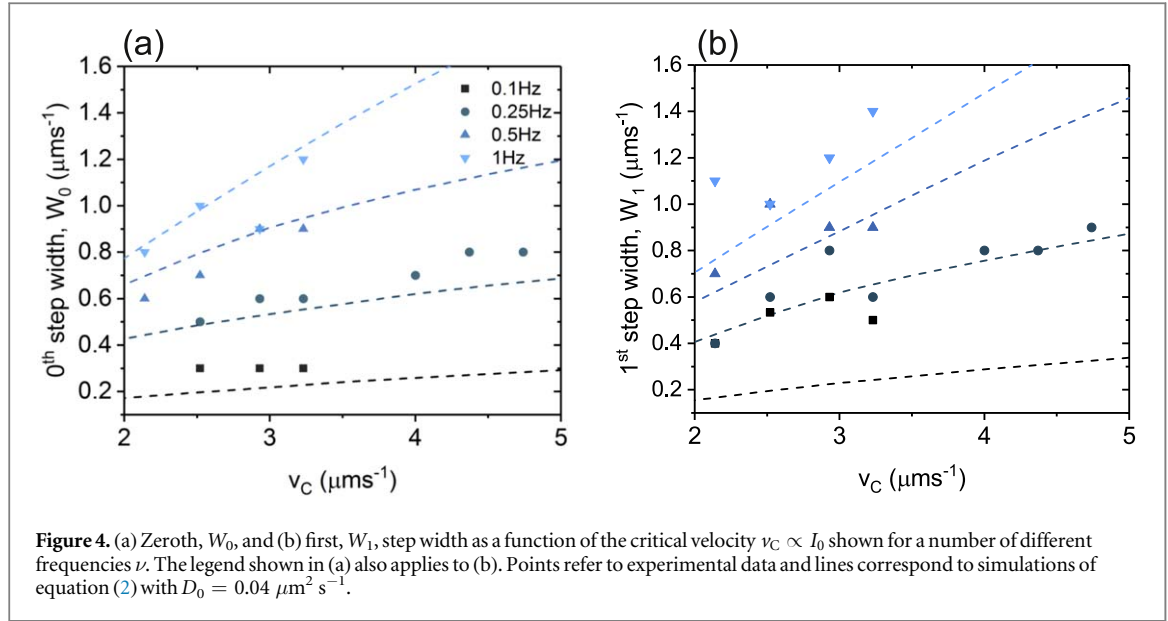
4.1. Average velocity experiments

First, we discuss the general behaviour of the average velocity of a sphere driven through a temporally oscillating optical landscape as a function of the driving velocity, which is summarised in figure 2, where we show the results from a single experiment with $I_0 = 480$ mW , and $\nu = 0.25$ Hz . Note that this laser power approximately corresponds to a critical velocity $v_{\mathrm{C}} = F_{\mathrm{C}} / \zeta = 4.6 \ \mu$m s^{-1}. First, there is a general increase in average velocity as the driving velocity is increased. For $v_{\mathrm{DC}} < 0.8 \ \mu$m s^{-1}, the particle remains stationary despite having an applied driving velocity, because the driving velocity is not high enough for the particle to move to the subsequent potential well within an oscillation. For $v_{\mathrm{DC}} > 0.8 \ \mu$m s^{-1}, the particle begins to move with a finite velocity. The average velocity increases until $v_{\mathrm{DC}} = 1.5 \ \mu$m s^{-1}, at which point it reaches a plateau up to $v_{\mathrm{DC}} = 2.4 \ \mu$m s^{-1} at $v_{\mathrm{AV}} = \lambda\nu = 0.875 \ \mu$m s^{-1}. In this range of driving velocities, the particle is mode locked and every oscillation of

Figure 2. (a) A plot of average velocity against driving velocity for a sphere passing through an oscillating optical landscape for $\lambda = 3.5\ \mu m$ and $\nu = 0.25$ Hz. Data points show experimental results for laser power $I_0 = 480$ mW whilst the solid line denotes simulation results according to equation (2) for $v_C = 4.6\ \mu m\ s^{-1}$ and with $D_0 = 0.04\ \mu m^2\ s^{-1}$. Dashed horizontal lines show the location of the first two mode locked steps. (b) $v_{DC} = 2.0\ \mu m\ s^{-1}$ and (c) $v_{DC} = 3.3\ \mu m\ s^{-1}$ show trajectories of points highlighted in (a), which correspond to the first and second mode locked steps. (d) and (e) show phase portraits for the trajectories shown in (b) and (c). Points show experimental data and lines show simulated results.

Figure 3. Schematic showing the mechanism for motion at the first mode locked step (left hand side), and the second mode locked step (right hand side). Bold particles show the instantaneous position with a shadow in place of initial particle position.

the optical landscape corresponds to the particle crossing to the adjacent potential well, as displayed in figure 2(b).

As the driving velocity is further increased, the average velocity also increases until $v_{DC} = 3.0\ \mu m\ s^{-1}$ where the second mode locked step is reached with $v_{AV} = 2\lambda\nu = 1.75\ \mu m\ s^{-1}$. In this mode, each time the optical landscape oscillates, the particle traverses two optical minima as displayed in figure 2(c). Note that in both individual particle trajectories, shown in figures 2(b) and (c), the particle remains stationary for approximately half of the overall oscillation time, corresponding to the optical landscape being at, or close to, its maximum depth. A schematic summary of the hopping behaviour at the first and second mode locked steps is shown in figure 3. For higher driving velocities, $v_{DC} > 3.4\ \mu m\ s^{-1}$, the average velocity increases nearly linearly with driving velocity. At these higher driving velocities, $F_{DC} \gg F_{opt}$, meaning that the landscape is relatively shallow. Effectively, the particle does not feel the landscape any more and experiences the dominating constant force only, therefore, $v_{AV} \rightarrow v_{DC}$. The absence of higher order mode locked steps is reminiscent of a high frequency regime, where the external frequency ν is high compared to the internal frequency v_C/λ, see appendix. In this limit, only the zeroth and first mode locked step are expected to be present.

Also shown in figure 2(a) are the numerical predictions from the simulations of the Langevin equation (2), which are in good agreement with the experimental data and accurately reproduce both the average velocity and

Figure 4. (a) Zeroth, W_0, and (b) first, W_1, step width as a function of the critical velocity $v_C \propto I_0$ shown for a number of different frequencies ν. The legend shown in (a) also applies to (b). Points refer to experimental data and lines correspond to simulations of equation (2) with $D_0 = 0.04 \ \mu\mathrm{m}^2 \ \mathrm{s}^{-1}$.

the width of the various mode locking steps. The simulations also suggest the presence of a third mode locking step. In comparision to steps 0 and 1, this third step is very narrow and because it is also masked by thermal fluctuations, it could not be resolved in the experiments. Further simulations performed at lower frequencies indicate that steps 0 and 1 start to shrink with decreasing frequency, see also section 4.3.
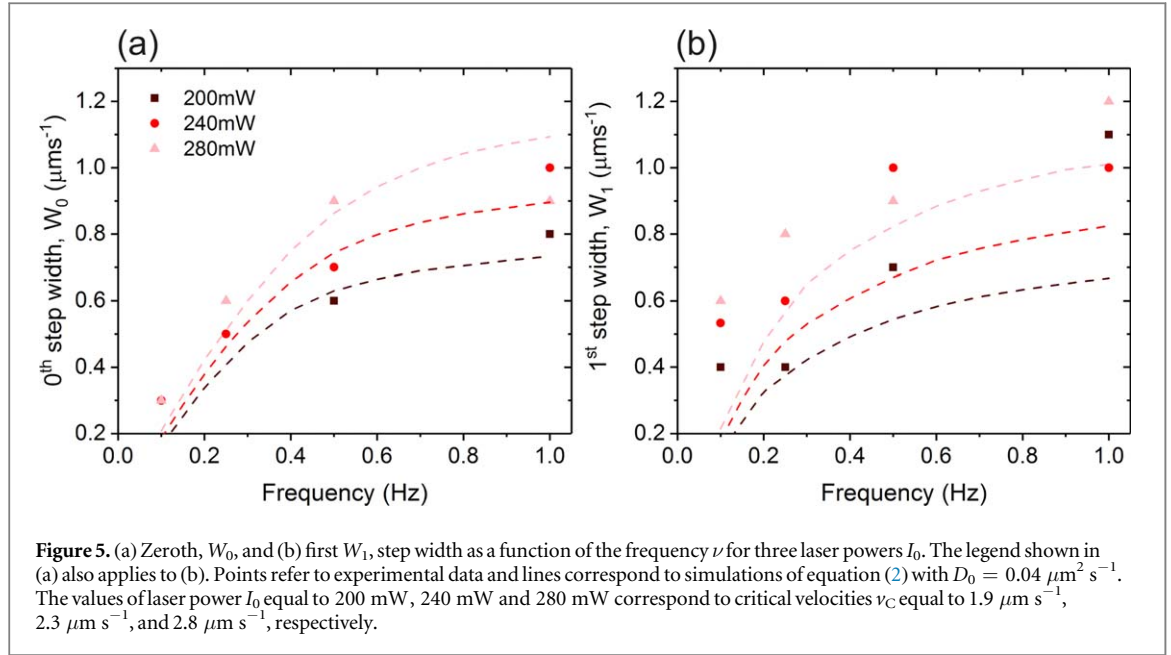
4.1.1. Phase portraits

To better visualise the nature of the mode locking observed in figure 2(a), phase portraits [29] are plotted from the particle trajectories corresponding to the first and second mode locked steps as shown in figures 2(d) and (e). Here, removing the mean drift from the particle trajectory, the phase is defined as $\varphi(t) = k[x(t) - \langle x(t)\rangle]$. The plot of $\mathrm{d}\varphi(t)/\mathrm{d}t$ against $\varphi(t)$, termed the phase portrait, shows the phase trajectory. For synchronised or mode locked motion, the deterministic phase trajectory is closed, corresponding to frequency locking $\nu_{AV} = n\nu$ (or, equivalently, $\nu_{AV} = n\lambda\nu$, see section 2.2) and implying phase locking, $\varphi(t) = n\omega t + \mathrm{const}$.

The phase portrait for the first mode locked step at $v_{DC} = 2.0 \ \mu\mathrm{m} \ \mathrm{s}^{-1}$, obtained by averaging data over 10 oscillations of the optical landscape, exhibits a closed loop due to the periodic motion of the particle, with the particle moving forward one trap spacing per oscillation. This can be compared to the phase portrait for a particle driven at $v_{DC} = 3.3 \ \mu\mathrm{m} \ \mathrm{s}^{-1}$, which corresponds to the second mode locked step and is shown in figure 2(e). Here a closed loop as a result of periodic particle motion is again observed, but each closed loop corresponds to the particle moving forward two trap spacings. The experimental results in figures 2(d) and (e) are compared to simulation results which fit well apart from at high values of both phase and phase velocity (top right quadrant) where the precise particle motion differs slightly. The simulation results correspond to the numerical solution of equation (2) without thermal noise, $\xi(t) = 0$, for the particle trajectory $x(t)$ from which the phase portrait is obtained as described above. Note that the simulations indeed show the closed loop nature of the phase portrait inherent to mode locked motion.

4.2. Laser power effects

Section 4.1 provides the general picture of dynamic mode locking at a given laser power and frequency. We now discuss how the zeroth and first step widths change with laser power I_0 for a number of different frequencies, see figure 4. For the sake of comparison of experimental data and simulations, we choose the critical velocity, $v_C = F_C/\zeta$, as the control parameter, which is equivalent to changing the laser power since $v_C \propto I_0$.

Figure 4(a), where we show experimental data (points) along with results of simulations (lines), presents the dependence of zeroth step width W_0 on the critical velocity, v_C. Since we consider only positive values of v_{DC}, the zeroth step width is simply equal to the critical velocity. The step width W_0 generally grows with increasing laser power. This is because increasing the laser power enhances the coupling between the oscillating optical landscape and the particle motion, which means that they can synchronise over a greater region of driving velocities leading to a wider mode locked step. From the theoretical perspective, the step width grows with an increasing critical velocity, v_C, as supported by simulations. This step width increase is consistent with the deterministic high-frequency theory, which predicts for the zeroth step width $W_0 = v_C/2$, see equation (A.10). Finally, we also inspect the laser power effect on the first step width, W_1, which is plotted in figure 4(b). Although

Figure 5. (a) Zeroth, W_0, and (b) first W_1, step width as a function of the frequency ν for three laser powers I_0. The legend shown in (a) also applies to (b). Points refer to experimental data and lines correspond to simulations of equation (2) with $D_0 = 0.04 \ \mu\text{m}^2 \ \text{s}^{-1}$. The values of laser power I_0 equal to 200 mW, 240 mW and 280 mW correspond to critical velocities v_C equal to 1.9 $\mu\text{m s}^{-1}$, 2.3 $\mu\text{m s}^{-1}$, and 2.8 $\mu\text{m s}^{-1}$, respectively.

the agreement with the simulations is not as good as for the zero step width, W_0, the general increase of W_1 with v_C is in qualitative agreement with the high-fequency theory, which predicts that $W_1 = v_C/2$, see equation (A.14).

4.3. Frequency effects

We now fix the laser power and analyse how the step widths of the observed mode locking steps change with the frequency. The comparison of the experimental data with the numerical results is presented in figure 5. The frequency dependence of the zeroth step width, W_0, for three values of I_0 is shown in figure 5(a), and as could already be expected from figure 4, it is clear that the zeroth step width increases with frequency. A particle must overcome the optical landscape to give a non-zero average velocity and this movement occurs when the landscape is at its most shallow, at $t \approx 1/(2\nu)$ (see figure 1). The time period in which the optical landscape is close to this 'shallow' state is inversely proportional to the frequency. This means that at low frequencies, where this time period is longest, the particle can move with least hindrance, leading to a smaller zeroth step width. Hence, the zeroth step width $W_0 \to 0$ as $\nu \to 0$. In the high frequency regime outlined in appendix, the deterministic zeroth step width $W_0 = v_C/2$, see equation (A.10), which ranges from 0.95 to 1.4 $\mu\text{m s}^{-1}$ for the laser powers used here. While the high frequency regime has not been fully reached, the observed step widths appear to be plateauing towards higher frequencies suggesting that the highest frequency used here, $\nu = 1$ Hz , can be approximated well by the high frequency regime. Note, however, that the deterministic predictions overestimate the experimentally observed values of the step widths, which is inherent to the absence of thermal fluctuations in the deterministic high frequency theory, and such these predicted values should be considered as upper bounds for the step widths in the limit $\nu \to \infty$.

Next, the frequency dependence of the first step width, W_1, is shown in figure 5(b). This shows a similar behaviour to that of the zeroth step, as the step width increases with frequency. At low frequencies, many closely spaced mode locked steps are expected with a separation of $\lambda\nu$. This means that the first step is inherently small as a large number of steps span a small range of v_{DC}. Tending towards a higher frequency leads to an increase in the step width, and in the high-frequency limit, the step width is again predicted to be $W_1 = v_C/2$ according to equation (A.14). This is observed for $I_0 = 200$ mW $(v_C = 1.9 \ \mu\text{m s}^{-1})$, and is closely approached for higher values of v_C, again suggesting that at $\nu = 1$ Hz , particle motion can be approximated well by the high frequency regime.

Experimentally it is challenging to probe step widths for $n \geqslant 2$ where the step width is on the order of experimental resolution. As this can, however, be probed in simulation, we now numerically explore how the second step width W_2 changes with frequency for a landscape with $v_C = 4.6 \ \mu\text{m s}^{-1}$, which corresponds to the data shown in figure 2. The results of sumulations for the frequency dependence of W_2 are shown in figure 6. At low frequencies, W_2 increases with the frequency similar to the behaviour of W_0 and W_1. Its growth, however, gradually decreases until W_2 peaks at $\nu \approx 0.3$ Hz . Beyond this value, the step width W_2 starts to reduce with frequency. This trend at high frequencies is in line with the deterministic high-frequency theory, which predicts $W_2 = 0$ in the high-frequency limit, $\nu \to \infty$. Thus, in contrast to steps 0 and 1, the second step is hard to detect
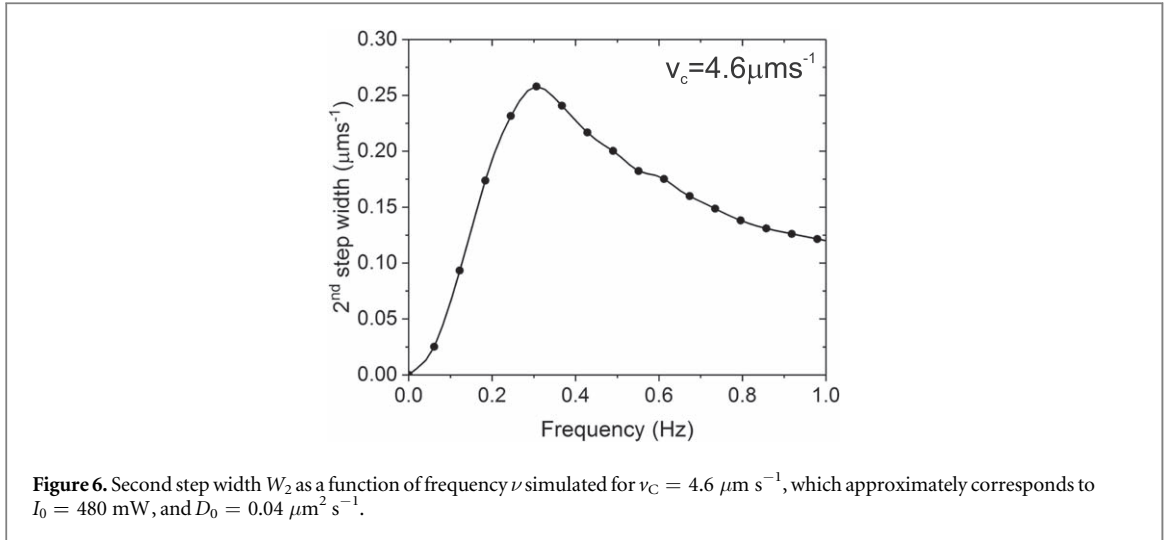
Figure 6. Second step width W_2 as a function of frequency ν simulated for $\nu_C = 4.6$ μm s^{-1}, which approximately corresponds to $I_0 = 480$ mW, and $D_0 = 0.04$ μm^2 s^{-1}.
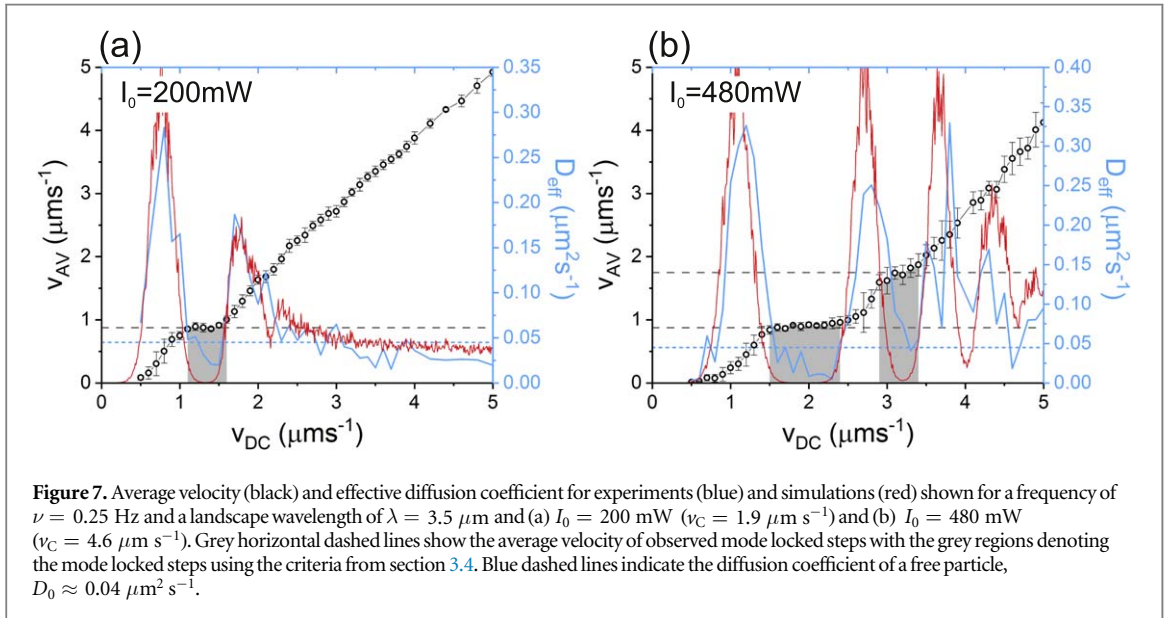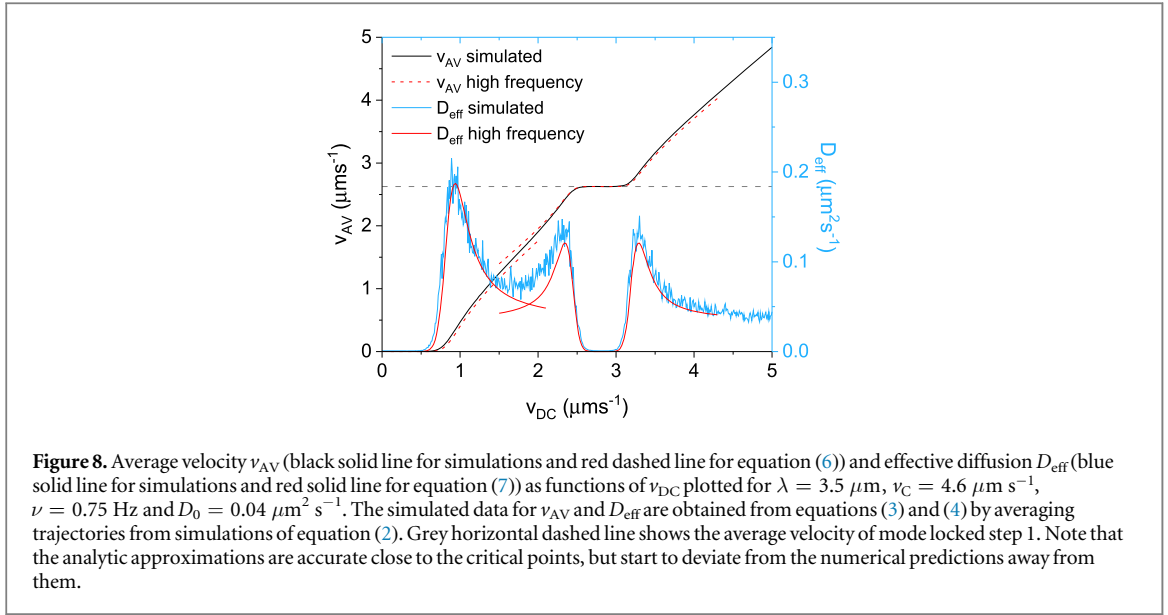

Figure 7. Average velocity (black) and effective diffusion coefficient for experiments (blue) and simulations (red) shown for a frequency of $\nu = 0.25$ Hz and a landscape wavelength of $\lambda = 3.5$ μm and (a) $I_0 = 200$ mW ($\nu_C = 1.9$ μm s^{-1}) and (b) $I_0 = 480$ mW ($\nu_C = 4.6$ μm s^{-1}). Grey horizontal dashed lines show the average velocity of observed mode locked steps with the grey regions denoting the mode locked steps using the criteria from section 3.4. Blue dashed lines indicate the diffusion coefficient of a free particle, $D_0 \approx 0.04$ μm^2 s^{-1}.

as its width, W_2, exhibits a maximum in a finite range of frequencies and is generally smaller than W_0 and W_1. As such, it is noteworthy that at $\nu = 0.25$ Hz $W_2 \approx 0.24$ μm s^{-1} is close to its maximum width while not being too much smaller than W_0 and W_1 at this frequency, which explains why the second step is observable in figure 2.

4.4. Effective diffusion coefficient

Finally, we study the effective diffusion coefficient of a particle moving across a temporally oscillating optical landscape. The average velocity and the effective diffusion coefficient are calculated from equations (3) and (4), respectively. Both quantities are plotted against the driving velocity ν_{DC} for two different values of laser power I_0 in figure 7.

In both plots, we see that an initial rise in the average velocity corresponds to a sharp rise in the effective diffusion coefficient as the particle begins to exhibit a non-zero velocity. Upon approaching the first mode locked step at $\nu_{DC} = 1.1$ μm s^{-1} in figure 7(a), the effective diffusion coefficient is greatly reduced. This is due to the periodic motion that a particle experiences when it is mode locked, leading to very low levels of effective diffusion. The effective diffusion coefficient even drops below the diffusion coefficient measured for a free particle, $D_0 = k_B T / \zeta \approx 0.04$ μm^2 s^{-1}, indicating that Brownian fluctuations are less significant on this mode locked step than for a free particle. As the driving velocity is increased beyond $\nu_{DC} = 1.6$ μm s^{-1}, the particle is no longer mode locked, and the effective diffusion coefficient rises again before slowly decreasing as the driving velocity increases beyond $\nu_{DC} = 1.7$ μm s^{-1}, where the optical landscape has a diminishing effect on the particle motion.

Figure 8. Average velocity v_{AV} (black solid line for simulations and red dashed line for equation (6)) and effective diffusion D_{eff} (blue solid line for simulations and red solid line for equation (7)) as functions of v_{DC} plotted for $\lambda = 3.5\ \mu$m, $v_C = 4.6\ \mu$s^{-1}, $\nu = 0.75$ Hz and $D_0 = 0.04\ \mu$m^2 s^{-1}. The simulated data for v_{AV} and D_{eff} are obtained from equations (3) and (4) by averaging trajectories from simulations of equation (2). Grey horizontal dashed line shows the average velocity of mode locked step 1. Note that the analytic approximations are accurate close to the critical points, but start to deviate from the numerical predictions away from them.

In figure 7(b), which shows results for a higher v_C, the effective diffusion coefficient exhibits similar behaviour for the first mode locked step as that seen in figure 7(a) but there is now a second mode locked step. At higher velocities this second mode locked step causes another drop in the effective diffusion coefficient between $v_{DC} = 2.9$–$3.4\ \mu$m s^{-1}. Simulated data shown in red correlate well with the experimental results, though further reductions in the effective diffusion coefficient are seen. These plots show that when a particle is mode locked, its motion is greatly restricted and in many cases leads to an effective diffusion coefficient that is even lower than that of a freely diffusing particle.

To gain further insights into the behaviour of the effective diffusion coefficient, we will make use of the predictions of the high-frequency theory (appendix). By comparing these predictions with those from simulations, we will now show that the behaviour of a particle in the temporally oscillating potential at and close to mode locking is similar to the Brownian motion in an effective stationary potential.

Consider Brownian motion of a colloidal particle in an effective time-independent potential that describes the dynamics at and close to mode-locked step n at high frequencies, see appendix:

$$\frac{U_{\text{eff}}^{(n)}(x)}{k_B T} = -\frac{\Delta v_n'}{D_0}x - \frac{\alpha_n v_C}{kD_0}\cos kx. \tag{5}$$

Here, the constants $\Delta v_n'$ and α_n are different for different steps, as given by equations (A.5) and (A.6). By adapting known results for the average velocity [43] and effective diffusion [45], close to steps $n = 0$ and 1, we arrive at the corresponding expressions

$$v_{\text{AV}}^{(n)} = n\lambda\nu + \frac{2D_0}{\lambda}\frac{\sinh(\pi\kappa_n)}{|I_{i\kappa_n}(\gamma_n)|^2} \tag{6}$$

and

$$D_{\text{eff}}^{(n)} = D_0 \frac{\int_0^\lambda \mathcal{I}_+^2(x)\mathcal{I}_-(x)\,dx}{\left[\int_0^\lambda \mathcal{I}_+(x)\,dx\right]^3}, \tag{7}$$

where $\kappa_n = \Delta v_n'/(kD_0)$, $\gamma_n = \alpha_n v_C/(kD_0)$, $\mathcal{I}_\pm(x) = \lambda^{-1}\int_0^\lambda \exp[\pm(U_{\text{eff}}^{(n)}(x) - U_{\text{eff}}^{(n)}(x \mp y))/k_B T]\,dy$, and $I_{ix}(y)$ is the modified Bessel function of the first kind.

As follows from expression (A.13), not only the width but also the location of step 1 grows with the frequency, ν. Thus, by considering higher frequencies, we increase the separation between steps 0 and 1 and the predictions of high-frequency theory become more reliable. For the comparison with simulations we therefore choose a frequency of $\nu = 0.75$ Hz. The corresponding results for the effective diffusion coefficient and the average velocity plotted as functions of the driving velocity, v_{DC}, are shown in figure 8. We see that at this frequency the peaks in the effective diffusion coefficient associated with the end of step 0 and the onset of step 1 remain separated, unlike the single peak in D_{eff} between steps 0 and 1 observed at $\nu = 0.25$ Hz in figure 7. Note that the predictions of the high-frequency theory for both the average velocity (6) and effective diffusion (7) are in excellent agreement with the results of numerical simulations. The latter is not accidental because the

time-averaged equations (A.5) are obtained up to a finite-frequency correction of order $\mathcal{O}(\nu^{-1})$. Their accuracy goes beyond the high-frequency limit, $\nu \to \infty$, which captures the terms up to order $\mathcal{O}(\nu^0)$.

Similarly to figure 7, we see that, due to synchronisation, the diffusion of the particle is strongly suppressed at the mode locked steps, where it drops to zero exponentially fast. The particle is trapped by the landscape and the dynamics are essentially deterministic. Close to the ends of the steps the diffusivity quickly starts to grow outwards and significantly exceeds the value of the free diffusivity. The maxima are achieved close to the critical points, $\nu_{\mathrm{DC},0}^{\mathrm{crit},+}$ for step 0 and $\nu_{\mathrm{DC},1}^{\mathrm{crit},\pm}$ for step 1. These values are slightly different from the deterministic predictions, see equations (A.9) and (A.13), due to thermal noise. Here, the tilt of the landscape reduces the potential barrier of the optical landscape, and the particle easily escapes from a given well to the subsequent well assisted by thermal noise, effectively increasing the diffusivity. Away from the steps, the presence of the landscape becomes less relevant and the particle tends to exhibit free Brownian motion as one moves away from the step. However, this remains only true in the case of perfectly separated steps. In our typical experimental situation this condition is not well fulfilled and the peaks in the effective diffusion coefficient corresponding to the neighbouring critical points start to interfere. This is clearly seen from comparing the results of the simulations for $\nu = 0.75$ Hz plotted against the predictions of the reduced model with an effective potential, in figure 8, to those in figure 7 for $\nu = 0.25$ Hz, where steps 0 and 1 are much closer. As a result, in the latter case the corresponding diffusion peaks cannot be resolved and collapse into a single peak between the steps.

5. Conclusions

In this work, a colloidal sphere has been driven across a temporally oscillating one-dimensional optical potential energy landscape. Particle motion was seen to exhibit dynamic mode locking corresponding to periodic particle motion. This was visualised for the $(1, 0)$ and $(2, 0)$ modes with the use of phase portraits. The effect of the laser intensity, and hence ν_{C}, on the step width was probed and was shown to have a high correlation with the zeroth step width, however, the first step width was shown to have a weaker dependence. The effect of the oscillation frequency on the step width was also studied and shown to be in line with a high-frequency theory for both experiments and simulations. Furthermore, the effective diffusion coefficient was investigated and was seen to be greatly reduced for a driving velocity corresponding to a mode locked step. Finally, the effective diffusion was studied numerically and compared to deterministic predictions for the high frequency regime where excellent agreement was observed.

Acknowledgments

Appendix. High-frequency theory

To obtain analytical insights into transport properties, here we consider the special case of high frequencies, where the external frequency ν is high compared to the internal frequency ν_{C}/λ, in which the equations of motion can be simplified close to mode locking by means of time averaging.

We start by neglecting thermal fluctuations in equation (2) and writing it in terms of velocities

$$\frac{\mathrm{d}x}{\mathrm{d}t} = v_{\mathrm{DC}} - \frac{v_{\mathrm{C}}}{2}(1 + \cos \omega t)\sin kx, \tag{A.1}$$

where $v_{\mathrm{DC}} = F_{\mathrm{DC}}/\zeta$ and $v_{\mathrm{C}} = F_{\mathrm{C}}/\zeta$. In such a system, we expect mode locked (or synchronised) motion [35] and will focus on the description of transport properties at and close to mode locked (Shapiro) steps. At step n, the particle is known to move with the average velocity $n\lambda\nu$ [28, 29], which suggests an ansatz for the coordinate

$$x(t) = n\lambda\nu t + \Delta x(t). \tag{A.2}$$

Here, the first term on the right hand side is the averaged solution on mode locked step n and the second term, $\Delta x(t)$, denotes the deviation from it which becomes increasingly non-zero as we move away from the step. Applying this ansatz to equation (A.1), expanding $\sin(n\omega t + k\Delta x)$, and taking account of trigonometric identities $2\sin(n\omega t)\cos(\omega t) = \sin[(n + 1)\omega t] + \sin[(n - 1)\omega t]$ and $2\cos(n\omega t)\cos(\omega t) = \cos[(n + 1)\omega t] + \cos[(n - 1)\omega t]$, for the dynamics close to step n we obtain an equation

$$\frac{d(\Delta x)}{dt} = \Delta\nu_n - \frac{\nu_C}{2}(1 + \cos\omega t)\sin(n\omega t + k\Delta x)$$

$$= \Delta\nu_n - \frac{\nu_C}{4}[\cos(k\Delta x)S_n(t) + \sin(k\Delta x)C_n(t)] \tag{A.3}$$

with $\Delta\nu_n = \nu_{DC} - n\lambda\nu$ and functions $S_n(t) = \sin[(n+1)\omega t] + 2\sin(n\omega t) + \sin[(n-1)\omega t]$ and $C_n(t) = \cos[(n+1)\omega t] + 2\cos(n\omega t) + \cos[(n-1)\omega t]$. Up to this point, we have made no approximations.

To make analytical progress, we now proceed to time averaging of this equation. We assume that the dynamics can be decomposed into slow (averaged) and fast (oscillatory) motion, and therefore $\Delta x(t) = q + \tilde{q}$, where q denotes $\Delta x(t)$ averaged over the time period of oscillation and $\tilde{q}$ contains explicit dependence on the oscillatory timescale ωt and multiples of it. Hereafter, the overbar is used to denote the time averaging. Similarly, we decompose $S = \bar{S} + \tilde{S}$ and $C = \bar{C} + \tilde{C}$. Because generally $\tilde{q} \to 0$ as $\omega \to \infty$, for high but finite frequencies it is natural to assume that $|\tilde{q}| \ll |q|$. Therefore, we can approximate $\cos(k\Delta x) \approx \cos kq - k\tilde{q}\sin kq$ and $\sin(k\Delta x) \approx \sin kq + k\tilde{q}\cos kq$ in equation (A.3). Further, finding a closed solution for the oscillatory part $\tilde{q}$ allows us to obtain a time averaged equation for the slowly evolving q.

First, keeping the leading oscillatory terms only in equation (A.3), we arrive at the equation that governs the fast dynamics, $d\tilde{q}/dt = -(\nu_C/4)[\tilde{S}_n(t)\cos kq + \tilde{C}_n(t)\sin kq]$. Taking into account that the slow evolution in $q(t)$ is indepenent of fast oscillatory dynamics, we integrate the above equation to obtain the explicit solution for $\tilde{q}(t)$

$$\tilde{q}(t) = \frac{\nu_C}{4\omega}[\tilde{c}_n(t)\cos kq - \tilde{s}_n(t)\sin kq], \tag{A.4}$$

where $\tilde{s}_n(t)$ and $\tilde{c}_n(t)$ are determined by oscillatory parts of the expressions $s_n(t) = (n+1)^{-1}\sin[(n+1)\omega t] + 2n^{-1}\sin(n\omega t) + (n-1)^{-1}\sin[(n-1)\omega t]$ and $c_n(t) = (n+1)^{-1}\cos[(n+1)\omega t] + 2n^{-1}\cos(n\omega t) + (n-1)^{-1}\cos[(n-1)\omega t]$. A careful consideration of the special cases for $n = 0, \mp 1$, at which the terms $\propto n^{-1}, (n\pm 1)^{-1}$ become formally singular, shows their actual absence in the corresponding definitions of $s_n(t)$ and $c_n(t)$. Therefore, our general analysis for arbitrary n remains valid under the convention that every singular term is omitted. Note also that as follows from equation (A.4), the oscillatory solution decays with the growth in frequency as $\tilde{q}(t) \propto \omega^{-1}$, in accordance with the accepted assumption that $\tilde{q} \to 0$ as $\omega \to \infty$.

Next, we proceed to performing the time averaging of equation (A.3). Because the time averaging of mixed trigonometric terms is trivial, $\overline{\tilde{c}_n(t)\tilde{S}_n(t)} \equiv 0$, $\overline{\tilde{s}_n(t)\tilde{C}_n(t)} \equiv 0$, the slow timescale dynamics is governed by the equation

$$\frac{dq}{dt} = \Delta\nu_n - \frac{\nu_C}{4}(\bar{S}_n\cos kq + \bar{C}_n\sin kq) - \frac{\nu_C^2 k}{16\omega}Q,$$

with $Q = \overline{\tilde{c}_n(t)\tilde{C}_n(t)}\cos^2 kq + \overline{\tilde{s}_n(t)\tilde{S}_n(t)}\sin^2 kq$ evaluated by noticing that $\overline{\tilde{c}_n(t)\tilde{C}_n(t)} = \overline{\tilde{s}_n(t)\tilde{S}_n(t)} = (n+1)^{-1}\overline{\sin^2[(n+1)\omega t]} + 4n^{-1}\overline{\sin^2(n\omega t)} + (n-1)^{-1}\overline{\sin^2[(n-1)\omega t]} = [(n+1)^{-1} + 4n^{-1} + (n-1)^{-1}]/2$. As directly follows from the definitions of $S_n(t)$ and $C_n(t)$, we have $\bar{S}_n = 0$ for all $n \geqslant 0$, and $\bar{C}_0 = 2$, $\bar{C}_1 = 1$ and $\bar{C}_n = 0$ for all $n \geqslant 2$.

As a result, the slow timescale evolution obeys a simple equation

$$\frac{dq}{dt} = \Delta\nu_n' - \alpha_n\nu_C\sin kq, \qquad \Delta\nu_n' = \nu_{DC} - n\lambda\nu - \frac{\delta_n\nu_C^2}{\lambda\nu} \tag{A.5}$$

with the coefficients

$$\alpha_n = \begin{cases} 1/2 & n = 0, \\ 1/4 & n = 1, \\ 0, & n \geqslant 2 \end{cases} \quad \delta_n = \begin{cases} 0 & n = 0, \\ 9/64 & n = 1, \\ \frac{3n^2-2}{16n(n^2-1)}. & n \geqslant 2 \end{cases}. \tag{A.6}$$

The time averaged equations allow a simple interpretation for transport properties. We note that the correction $\delta_n\nu_C^2/(\lambda\nu)$, which describes a small shift of the mode-locked steps, vanishes in the high-frequency limit $\nu \to \infty$ corresponding to approximation $\tilde{q}(t) = 0$ in equation (A.4). Requiring smallness of this correction in comparison with the term $\lambda\nu$ specifies the validity condition of the high-frequency approximation. For example, for the most interesting case $n = 1$ we find the criterium of high frequency to be $\nu \gg 3\nu_C/(8\lambda)$. We now consider the transport properties in more detais.

A.1. Zeroth mode locked step

For $n = 0$, we have $\Delta\nu_0 = \nu_{DC}$, $x(t) = q(t)$, and equation (A.5) reduces to

$$\frac{dx}{dt} = \nu_{DC} - \frac{\nu_C}{2}\sin kx, \tag{A.7}$$

which leads to the average velocity close to the zeroth mode locked summarised as [43]

$$v_{\mathrm{AV}}^{(0)} = \begin{cases} 0, & 0 \leqslant v_{\mathrm{DC}} \leqslant v_{\mathrm{C}}/2 \\ \sqrt{v_{\mathrm{DC}}^2 - (v_{\mathrm{C}}/2)^2}, & v_{\mathrm{DC}} > v_{\mathrm{C}}/2. \end{cases} \tag{A.8}$$

The critical velocity corresponds to the situation when the two branches of equation (A.8) coincide. This happens when the square root vanishes, and we obtain

$$v_{\mathrm{DC},0}^{\mathrm{crit},\pm} = \pm \frac{v_{\mathrm{C}}}{2}. \tag{A.9}$$

Since we consider only positive values of v_{DC}, the width of step 0 corresponds to

$$W_0 = v_{\mathrm{DC},0}^{\mathrm{crit},+} = \frac{v_{\mathrm{C}}}{2}. \tag{A.10}$$

A.2. First mode locked step

For $n = 1$, we have $\Delta v_1' = v_{\mathrm{DC}} - \lambda \nu - 9 v_{\mathrm{C}}^2/(64 \lambda \nu)$, the original coordinate $x(t) = \lambda \nu + q(t)$, and equation (A.5) yields

$$\frac{\mathrm{d}q}{\mathrm{d}t} = \Delta v_1' - \frac{v_{\mathrm{C}}}{4} \sin kx. \tag{A.11}$$

Similarly to the case, $n = 0$, this gives rise to an average velocity at, or close to, the mode locked step where $n = 1$

$$v_{\mathrm{AV}}^{(1)} = \begin{cases} \lambda \nu, & |\Delta v_1'| \leqslant v_{\mathrm{C}}/4 \\ \lambda \nu \pm \sqrt{(\Delta v_1')^2 - (v_{\mathrm{C}}/4)^2}, & |\Delta v_1'| > v_{\mathrm{C}}/4. \end{cases} \tag{A.12}$$

Note that depending on the frequency ν, the quantity $\Delta v_1'$ can take both positive and negative values, while v_{DC} remains non-negative. The critical velocities are determined by the vanishing square root, which yields

$$v_{\mathrm{DC},1}^{\mathrm{crit},\pm} = \lambda \nu + \frac{9 v_{\mathrm{C}}^2}{64 \lambda \nu} \pm \frac{v_{\mathrm{C}}}{4}. \tag{A.13}$$

Thus, the first mode locked step is centered at the value $\lambda \nu + 9 v_{\mathrm{C}}^2/(64 \lambda \nu)$ and has the width

$$W_1 = v_{\mathrm{DC},1}^{\mathrm{crit},+} - v_{\mathrm{DC},1}^{\mathrm{crit},-} = \frac{v_{\mathrm{C}}}{2}. \tag{A.14}$$

A.3. Higher order mode locked steps

For the case of $n \geqslant 2$, the time average of equation (A.5) is vastly simplified and only the first constant term remains,

$$\frac{\mathrm{d}q}{\mathrm{d}t} = \Delta v_n' = v_{\mathrm{DC}} - n \lambda \nu - \frac{(3n^2 - 2) v_{\mathrm{C}}^2}{16 n(n^2 - 1) \lambda \nu} \quad (n \geqslant 2). \tag{A.15}$$

This means that the optical potential is effectively vanishing, leading to the trivial result for the average velocity

$$v_{\mathrm{AV}}^{(n)} = v_{\mathrm{DC}} - \frac{\delta_n v_{\mathrm{C}}^2}{\lambda \nu}, \quad W_n = 0, \quad n \geqslant 2. \tag{A.16}$$

Hence, we find a step width of 0 for all $n \geqslant 2$. This is very different to what is seen for a mode locked system with an oscillating driving force [28, 29] where mode locking steps exits for all integer n, as has been experimentally observed for up to $n = 6$.

ORCID iDs

Roel P A Dullens ⓘ https://orcid.org/0000-0003-1751-0958

References

[1] Chakrabarti B K and Stinchcombe R B 1999 Stick-slip statistics for two fractal surfaces: A model for earthquakes *Physica* A **270** 27–34
[2] Li K W, Wu H H and Lin Y C 2006 The effect of shoe sole tread groove depth on the friction coefficient with different tread groove widths, floors and contaminants *Appl. Ergon.* **37** 743–8
[3] Patrikar R M 2004 Modeling and simulation of surface roughness *Appl. Surf. Sci.* **228** 213–20
[4] Yastrebov V A, Anciaux G and Molinari J F 2015 From infinitesimal to full contact between rough surfaces: evolution of the contact area *Int. J. Solids Struct.* **52** 83–102
[5] Franzosi P, Salviati G, Scaffardi M, Genova F, Pellegrino S and Stano A 1988 Cracks in InP-based heterostructures *J. Cryst. Growth* **88** 135–42

[6] Talkner P, Hershkovitz E, Pollak E and Hänggi P 1999 Controlling activated surface diffusion by external fields *Surf. Sci.* **437** 198–206

[7] Bohlein T, Mikhael J and Bechinger C 2012 Observation of kinks and antikinks in colloidal monolayers driven across ordered surfaces *Nat. Mater.* **11** 126–30

[8] Vanossi A and Tosatti E 2012 Colloidal friction: kinks in motion *Nat. Mater.* **11** 97–8

[9] Sprinkle M, Ruan M, Hu Y, Hankinson J, Rubio-Roy M, Zhang B, Wu X, Berger C and De Heer W A 2010 Scalable templated growth of graphene nanoribbons on SiC *Nat. Nanotechnol.* **5** 727–31

[10] Fustin C A, Glasser G, Spiess H W and Jonas U 2004 Parameters influencing the templated growth of colloidal crystals on chemically patterned surfaces *Langmuir* **20** 9114

[11] Sellier H, Baraduc C, Lefloch F and Calemczuk R 2004 Half-integer shapiro steps at the 0-pi crossover of a ferromagnetic josephson junction *Phys. Rev. Lett.* **92** 257005

[12] Reichhardt C, Scalettar R T, Zimányi G T and Grønbech-Jensen N 2000 Shapiro steps in driven vortex lattices interacting with periodic pinning arrays *Physica* C **332** 1–4

[13] Jelčić D, Bjeliš A and Batistić I 1988 Interference effects in nonlinear charge-density-wave dynamics *Phys. Rev.* B **38** 4045

[14] Carpinelli J M, Weitering H H, Plummer E W and Stumpf R 1996 Direct observation of a surface charge density wave *Nature* **381** 398–400

[15] Hanes R D L, Schmiedeberg M and Egelhaaf S U 2013 Brownian particles on rough substrates: relation between intermediate subdiffusion and asymptotic long-time diffusion *Phys. Rev.* E **88** 062133

[16] Su Y, Lai P Y, Ackerson B J, Cao X, Han Y and Tong P 2017 Colloidal diffusion over a quasicrystalline-patterned surface *J. Chem. Phys.* **146** 214903

[17] Su Y, Ma X G, Lai P Y and Tong P 2017 Colloidal diffusion over a quenched two-dimensional random potential *Soft Matter* **13** 4773–85

[18] Bewerunge J, Ladadwa I, Platten F, Zunke C, Heuer A and Egelhaaf S U 2016 Time- and ensemble-averages in evolving systems: the case of Brownian particles in random potentials *Phys. Chem. Chem. Phys.* **18** 18887–95

[19] Evers F, Zunke C, Hanes R D L, Bewerunge J, Ladadwa I, Heuer A and Egelhaaf S U 2013 Particle dynamics in two-dimensional random-energy landscapes: experiments and simulations *Phys. Rev.* E **88** 022125

[20] Evers F *et al* 2013 Colloids in light fields: particle dynamics in random and periodic energy landscapes *Eur. Phys. J. Spec. Top.* **222** 2995

[21] Choudhury U, Straube A V, Fischer P, Gibbs J G and Höfling F 2017 Active colloidal propulsion over a crystalline surface *New J. Phys.* **19** 125010

[22] Lindenberg K, Sancho J M, Lacasta A M and Sokolov I M 2007 Dispersionless transport in a washboard potential *Phys. Rev. Lett.* **98** 020602

[23] Sancho J M and Lacasta A M 2010 The rich phenomenology of Brownian particles in nonlinear potential landscapes *Eur. Phys. J. Spec. Top.* **187** 49–62

[24] Lacasta A M, Sancho J M, Romero A H, Sokolov I M and Lindenberg K 2004 From subdiffusion to superdiffusion of particles on solid surfaces *Phys. Rev.* E **70** 1–10

[25] Reimann P, Van den Broeck C, Linke H, Hänggi P, Rubi J M and Pérez-Madrid A 2001 Giant acceleration of free diffusion by use of tilted periodic potentials *Phys. Rev. Lett.* **87** 010602

[26] Tierno P, Johansen T H and Fischer T M 2007 Localized and delocalized motion of colloidal particles on a magnetic bubble lattice *Phys. Rev. Lett.* **99** 038303

[27] Soba A, Tierno P, Fischer T M and Saguès F 2008 Dynamics of a paramagnetic colloidal particle driven on a magnetic-bubble lattice *Phys. Rev.* E **77** 060401

[28] Juniper M P N, Zimmermann U, Straube A V, Besseling R, Aarts D G A L, Löwen H and Dullens R P A 2017 Dynamic mode locking in a driven colloidal system: experiments and theory *New J. Phys.* **19** 013010

[29] Juniper M P N, Straube A V, Besseling R, Aarts D G A L and Dullens R P A 2015 Microscopic dynamics of synchronization in driven colloids *Nat. Commun.* **6** 7187

[30] Abbott J L, Spiers J A, Gao Y, Aarts D G A L and Dullens R P A 2019 Colloidal rods in optical potential energy landscapes *J. Phys. D: Appl. Phys.* **52** 024002

[31] Milne G, Rhodes D, MacDonald M and Dholakia K 2007 Fractionation of polydisperse colloid with acousto-optically generated potential energy landscapes *Opt. Lett.* **32** 1144

[32] Xiao K and Grier D G 2010 Sorting colloidal particles into multiple channels with optical forces: prismatic optical fractionation *Phys. Rev.* E **82** 051407

[33] Korda P T, Taylor M B and Grier D G 2002 Kinetically locked-in colloidal transport in an array of optical tweezers *Phys. Rev. Lett.* **89** 128301

[34] Roichman Y, Wong V and Grier D G 2007 Colloidal transport through optical tweezer arrays *Phys. Rev.* E **75** 011407

[35] Romanczuk P, Müller F and Schimansky-Geier L 2010 Quasideterministic transport of Brownian particles in an oscillating periodic potential *Phys. Rev.* E **81** 061120

[36] Paronuzzi Ticco S V, Fornasier G, Manini N, Santoro G E, Tosatti E and Vanossi A 2016 Subharmonic Shapiro steps of sliding colloidal monolayers in optical lattices *J. Phys.: Condens. Matter* **28** 134006

[37] Brazda T, July C and Bechinger C 2017 Experimental observation of Shapiro-steps in colloidal monolayers driven across time-dependent substrate potentials *Soft Matter* **13** 4024

[38] Tierno P and Shaebani M R 2016 Enhanced diffusion and anomalous transport of magnetic colloids driven above a two-state flashing potential *Soft Matter* **12** 3398

[39] Martinez-Pedrero F, Massana-Cid H, Ziegler T, Johansen T H, Straube A V and Tierno P 2016 Bidirectional particle transport and size selective sorting of Brownian particles in a flashing spatially periodic energy landscape *Phys. Chem. Chem. Phys.* **18** 26353–7

[40] Straube A V and Tierno P 2013 Synchronous versus asynchronous transport of a paramagnetic particle in a modulated ratchet potential *Europhys. Lett.* **103** 28001

[41] Stoop R L, Straube A V and Tierno P 2019 Enhancing nanoparticle diffusion on a unidirectional domain wall magnetic ratchet *Nano Lett.* **19** 433–40

[42] Pikovsky A, Rosenblum M and Kurths J 2001 *Synchronization A Universal Concept in Nonlinear Sciences* (Cambridge: Cambridge University Press)

[43] Juniper M P N, Straube A V, Aarts D G A L and Dullens R P A 2016 Colloidal particles driven across periodic optical-potential-energy landscapes *Phys. Rev.* E **93** 012608

[44] Juniper M P N, Besseling R, Aarts D G A L and Dullens R P A 2012 Acousto-optically generated potential energy landscapes: potential mapping using colloids under flow *Opt. Express* **20** 28707

[45] Reimann P, Van den Broeck C, Linke H, Hänggi P, Rubi J M and Pérez-Madrid A 2002 Diffusion in tilted periodic potentials: enhancement, universality, and scaling *Phys. Rev.* E **65** 031104